

Infrared spectroscopy and time-resolved dynamics of the ortho- H_2 –OH entrance channel complex

David T. Anderson, Rebecca L. Schwartz, Michael W. Todd, and Marsha I. Lester

Citation: *The Journal of Chemical Physics* **109**, 3461 (1998); doi: 10.1063/1.476941

View online: <http://dx.doi.org/10.1063/1.476941>

View Table of Contents: <http://scitation.aip.org/content/aip/journal/jcp/109/9?ver=pdfcov>

Published by the [AIP Publishing](#)

Articles you may be interested in

[OD–N₂ : Infrared spectroscopy, potential anisotropy, and predissociation dynamics from infrared-ultraviolet double resonance studies](#)

J. Chem. Phys. **116**, 913 (2002); 10.1063/1.1425833

[Spectroscopy and dynamics of \$\text{I}_2\(\text{B}\)\$ –Ne](#)

J. Chem. Phys. **115**, 784 (2001); 10.1063/1.1378317

[Erratum: “The spectroscopy and IVR dynamics of HOCl in the \$\nu_{\text{OH}}=6\$ region, probed by infrared-visible double resonance overtone excitation” \[*J. Chem. Phys.* **111**, 123 \(1999\)\]](#)

J. Chem. Phys. **112**, 2569 (2000); 10.1063/1.480828

[The spectroscopy and intramolecular vibrational energy redistribution dynamics of HOCl in the \$\nu_{\text{OH}}=6\$ region, probed by infrared-visible double resonance overtone excitation](#)

J. Chem. Phys. **111**, 123 (1999); 10.1063/1.479258

[Spectroscopy and dynamics of the \$\text{H}_2\$ – CN van der Waals complex](#)

J. Chem. Phys. **109**, 5171 (1998); 10.1063/1.477132



Infrared spectroscopy and time-resolved dynamics of the ortho- H_2 -OH entrance channel complex

David T. Anderson, Rebecca L. Schwartz,^{a)} Michael W. Todd, and Marsha I. Lester
Department of Chemistry, University of Pennsylvania, Philadelphia, Pennsylvania 19104-6323

(Received 7 April 1998; accepted 27 May 1998)

The rotationally resolved infrared spectrum of the prereactive *o*- H_2 -OH complex in its ground electronic state is obtained in the OH overtone region at $\sim 1.4\ \mu\text{m}$ using an IR-UV double resonance fluorescence enhancement technique. The pure OH overtone band of *o*- H_2 -OH is observed as well as approximately 20 additional rovibrational transitions extending out to the OH ($X^2\Pi, v=2$) + *o*- H_2 ($X^1\Sigma_g^+$) dissociation limit. These transitions are assigned as combination bands involving the simultaneous excitation of the OH vibrational overtone and intermolecular bending (internal rotor) states. The assignment of the experimental spectrum is aided by a detailed comparison with the bound states computed for the *ab initio* potential of Clary, Werner, and co-workers [Mol. Phys. **83**, 405 (1994)]. The infrared spectroscopy results also verify the topology of this *ab initio* potential in the entrance channel to the OH+ H_2 hydrogen abstraction reaction. Direct time-resolved experiments indicate that the lifetime of the vibrationally activated *o*- H_2 -OH complex in the ground intermolecular state is 115(26) ns. The initial excitation is found to stay localized in the OH intramolecular stretching mode for a long period of time prior to vibrational predissociation or chemical reaction. © 1998 American Institute of Physics. [S0021-9606(98)01033-2]

I. INTRODUCTION

The OH+ H_2 → H_2O +H reaction is arguably the best-characterized four-atom reaction to date. It has been the topic of detailed kinetic rate measurements^{1–5} and molecular beam scattering studies,^{6,7} while the reverse reaction has been examined in a series of hot H-atom experiments.^{8,9} This reaction has also received intense theoretical attention and in recent years has become the benchmark for four-atom quantum mechanical reactive scattering calculations.^{10–25} While these calculations qualitatively reproduce much of the experimental results, the potential energy surface^{26,27} (PES) used for most of these studies is likely to require modifications. In particular, the transition state is believed to be too late and a “spurious well” is known to occur in the entrance channel of the fitted surface.^{10,11,28,29} This potential has been modified^{11,12} to remove some of these deficiencies, and new potential energy surfaces are becoming available³⁰ or are under development.⁷ While the PES clearly influences the dynamics of a reaction, the connection between the features of the PES and the reaction dynamics are often not obvious. As a result, there is a need for experimental measurements that can test specific regions of this multidimensional reactive PES. Reactive potentials tend to be most accurate near the transition state, but need to be checked along the entire minimum energy pathway. Electron photodetachment studies of the H_3O^- anion by Neumark, Lineberger, and co-workers have provided the first detailed information on the OH+ H_2 potential near the transition state of the reaction.³¹ These experiments probe the neutral reactive potential surface in regions that have Franck–Condon overlap with two isomeric

forms of the H_3O^- anion, $\text{H}^-(\text{H}_2\text{O})$ and $\text{OH}^-(\text{H}_2)$. The $\text{H}^-(\text{H}_2\text{O})$ isomer accesses the exit channel, while $\text{OH}^-(\text{H}_2)$ probes the entrance channel in the vicinity of the transition state.

A complimentary approach involves studying the spectroscopy and dynamics of the prereactive OH– H_2 complex. Spectroscopic experiments on this weakly bound complex furnish detailed information on the shape of the PES in the entrance channel to reaction. The OH– H_2 complex was first observed via electronic spectroscopy utilizing the strong OH $A^2\Sigma^+ - X^2\Pi$ electronic transition by Loomis and Lester in 1995.^{32–34} These studies revealed the surprising result that the reactants to this low-barrier, exothermic reaction could be trapped in a shallow intermolecular well located in the entrance channel to reaction. Since then, Schwartz *et al.*³⁵ recorded the pure OH overtone spectrum of OH– H_2 in the *ground* electronic state using an IR-UV fluorescence depletion technique. The rotationally resolved infrared spectrum provided strong spectroscopic evidence that binary complexes of *o*- H_2 -OH were the spectral carriers. Assignment of the experimental spectrum was aided by theoretical predictions of the infrared spectrum for *o*- H_2 -OH by Clary, Werner, and co-workers.³⁶ The agreement between experiment and theory was impressive, indicating that the *ab initio* PES used in these calculations was realistic in the vicinity of the potential minimum.

Intramolecular vibrational excitation of these prereactive complexes can also be used to study the inelastic and reactive half-collision dynamics of OH– H_2 . The high-frequency intramolecular modes ($\nu_{\text{H}_2} \approx 4150\ \text{cm}^{-1}$ and $\nu_{\text{OH}} \approx 3500\ \text{cm}^{-1}$) of OH– H_2 have more than sufficient energy to break the weak intermolecular bond (inelastic) and/or surmount the barrier to reaction (reactive). These processes are

^{a)}Current address: JILA, University of Colorado, Boulder, Colorado 80309-0440.

expected to be stereo- and mode-selective, and the time it takes the initially prepared vibrational state to decay should depend critically on the type of mode excited and the available product states. For example, vibrational excitation of the OH-stretch is not expected to strongly enhance reaction in the complex because both kinetic experiments^{3–5} and theoretical calculations^{10,11} have shown that the OH vibration is a “spectator” to reaction. In contrast, vibrational excitation of the H₂ molecule dramatically increases the reaction rate^{1,3,4,19} and, therefore, might directly initiate reaction in the weakly bound complex. By initiating the half-collision in a weakly bound complex, the reactants are restricted to a limited range of orientations. Intermolecular excitation can be used to manipulate the relative orientation of the reactants within the complex, and thereby sample configurations that closely resemble the transition state structure of the reaction. The half-collision dynamics resulting from vibrational activation of OH–H₂ will be sensitive to repulsive portions of OH+H₂ PES, including reactive regions.

In the present paper, the entrance channel of the OH+H₂ reaction is probed via rotationally resolved infrared overtone spectroscopy of the OH–H₂ prereactive complex. We present new experimental results on excited intermolecular bending (internal rotor) states of OH–H₂ and compare these results with high quality 4D quantum calculations of the bound rovibrational states calculated on two different *ab initio* potentials. This comparison provides a stringent test of the topology of the intermolecular potential in the entrance channel to reaction. In addition, the IR-UV double resonance detection scheme used in this work permits time-domain measurements of the lifetime of the vibrationally activated OH–H₂ complex. The lifetime of the $\nu_{\text{OH}}=2$ excited state reflects the time scale for energy to remain localized in the high frequency OH stretch prior to vibrational predissociation or reaction.

The paper is organized as follows: Sec. II gives a brief overview of the theoretical potentials developed for reactive and inelastic scattering studies of OH+H₂, including a theoretical description of the bound intermolecular states of OH–H₂. Section III describes the experimental techniques employed to record the infrared spectrum of OH–H₂. This section also contains a comparison of two different IR-UV double resonance schemes used to study OH–H₂, fluorescence depletion and fluorescence enhancement, with a discussion of the particular strengths and weaknesses of each method. The experimental results and tentative spectroscopic assignments are presented in Sec. IV. The time-resolved lifetime measurements for the $\nu_{\text{OH}}=2$ state of *o*-H₂–OH are discussed in Sec. V, along with an interpretation of the long lifetime observed. The spectroscopic results for the excited intermolecular bending levels are utilized to differentiate between two *ab initio* potentials for OH+H₂: the CEPA potential of Clary, Werner, and co-workers³⁶ (MCKW) and the SCF potential of Kochanski and Flower (KF).^{37,38} These two potentials, which were developed for bound state and inelastic scattering quantum calculations, are compared with the entrance channels of potentials used for reactive scattering. Finally, conclusions and plans for future work are presented in Sec. VI.

II. THEORETICAL BACKGROUND

A. Potential energy surfaces

For collinear geometries of OH–H₂, the OH($X^2\Pi$) + H₂($X^1\Sigma_g^+$) asymptote correlates with a single $^2\Pi$ electronic state (neglecting the spin–orbit interaction). At non-linear geometries, the degeneracy of this $^2\Pi$ state is lifted resulting in two surfaces, which for planar configurations of the complex (C_s symmetry) can be characterized as having $^2A'$ or $^2A''$ symmetry depending on whether the half-filled π -orbital of OH is in-plane or out-of-plane, respectively. At long range (3–10 Å) these two surfaces are close in energy, while at short range (1–3 Å) they can be widely separated, and this energy difference depends strongly on the relative orientation of the H₂ and OH moieties. Only the A' surface correlates adiabatically with the H+H₂O reaction products²⁶ and, therefore, all theoretical studies of the OH+H₂ reaction consider only the A' surface.

Theoretical studies of the reaction began in 1980 with the *ab initio* calculations (POL-CI/DZ+P) of Walch and Dunning,²⁶ which were subsequently used by Schatz and Elgersma (SE) to construct a global six-dimensional potential energy surface.²⁷ Extensive classical, semiclassical, and quantum dynamics studies have been published using the SE potential and accordingly this surface has served a pivotal role in the advancement of our understanding of this reaction.^{39,40} However, this fitted surface is now believed to have some serious flaws: the transition state is believed to be too late, and “spurious” wells and barriers have been identified in the entrance channel.^{10,11,28,29} More recent *ab initio* calculations (GVB-CI/TZ+P) by Kraka and Dunning⁴¹ have been fit by Isaacson³⁰ to construct a new PES (S5). The transition state region on the S5 surface is anticipated to be more accurate, but this surface has not yet been fully tested by quantum scattering calculations. In addition, another surface is being developed by Kliesch, Werner, and Clary using the CMRI+Q procedure with large basis sets.⁷ Early reports indicate this surface also has an improved transition state region.

The nuclear dynamics of the OH–H₂ entrance channel complex sample both the A' and A'' surfaces. Therefore, potentials that include both the reactive (A') and nonreactive (A'') surfaces are needed to calculate the bound states and infrared spectrum of OH–H₂. In 1981, Kochanski and Flower³⁷ calculated *ab initio* points (SCF) for both the A' and A'' surfaces as a function of the four intermolecular coordinates in order to interpret the OH($X^2\Pi$)+H₂ inelastic rotational scattering data. *Ab initio* potential energy points were calculated for seven angular orientations (all planar) at five different intermolecular separations (R) with the OH and H₂ bond lengths held fixed. These calculations rigorously treat both the A' and A'' adiabatic PESs in the entrance channel, but do not consider the reactive regions of the potential. The Kochanski and Flower *ab initio* data were later fit by Miller and Clary³⁸ to construct a 4D PES surface (KF), which has been used for inelastic scattering and bound state calculations. For computational convenience in the dynamics calculations, the two potential surfaces are expanded as average $V_{\text{AVG}} = \frac{1}{2}(V_{A''} + V_{A'})$ and difference $V_{\text{DIF}} = \frac{1}{2}(V_{A''} - V_{A'})$.

$-V_{A'})$ potentials. The KF potential is thought to overestimate the intermolecular well depth due to basis set superposition errors in the original *ab initio* data. Nevertheless, the KF potential was found to qualitatively reproduce the inelastic scattering data of Andresen and co-workers.^{42,43}

More recent *ab initio* calculations (CEPA) by Miller and co-workers³⁶ were performed at six planar configurations over a wider range of R separations (2–5 Å) to construct an improved 4D potential energy surface (MCKW) for both inelastic scattering and bound state calculations. The global minimum on the average surface ($V_{\text{AVG}} = -188.1 \text{ cm}^{-1}$) is located at a T-shaped OH–H₂ geometry where the A'' surface is $\sim 18 \text{ cm}^{-1}$ lower in energy than the A' surface. More accurate *ab initio* methods were employed in constructing the MCKW potential than the KF potential, and thus the MCKW potential is expected to be more reliable. Another potential has been developed by Offer and van Hemert⁴⁴ (OvH) that explicitly considers nonplanar configurations (where the A' and A'' symmetry labels are lost) and fits newly calculated *ab initio* points to a more flexible functional form. However, no bound state calculations have been published for the OvH potential so we restrict our attention in this paper to the MCKW and KF intermolecular potentials.

B. Bound intermolecular states of OH–H₂

The weakly bound OH–H₂ complex is predicted to exhibit large amplitude intermolecular bending and stretching motion even at the zero-point level.^{36,38} The rotational constants for H₂ and OH are both very large, and thus to first-order the majority of bound intermolecular states in the complex are best described as internal rotor states composed of different body-fixed projections of the lowest energy free rotor states of the constituent monomers. Unlike closed shell species, however, the theoretical description of OH–H₂ is complicated by interactions among the four different sources of angular momentum in the system. These include the angular momenta associated with the orbital and spin motions of the unpaired electron in OH, internal rotation of the H₂ and OH subunits, and the end-over-end rotation of the complex.

The large amplitude bending motion of OH and H₂ in the complex make it appropriate to use an angular momentum coupling scheme based on free-rotor quantum numbers, with OH treated in the Hund's case (a) limit. The angular momentum of OH (j_{OH}), the rotational angular momentum of H₂ (j_{H_2}), and the orbital angular momentum (L) of the complex are coupled together to give the total angular momentum J of the system ($J = j_{\text{OH}} + j_{\text{H}_2} + L$). The projection of J (or $j_{\text{OH}} + j_{\text{H}_2}$ since the projection of L must be zero) along the intermolecular axis (R) is labeled by K . Of these, only J is a true quantum number for the complex, although j_{OH} , j_{H_2} , and K are nearly conserved in OH–H₂, particularly at low intermolecular energies.

The two nuclear spin modifications for H₂ give rise to completely distinct *o*-H₂–OH and *p*-H₂–OH complexes, which have very different intermolecular energy level patterns. The intermolecular bending states of *p*-H₂–OH are

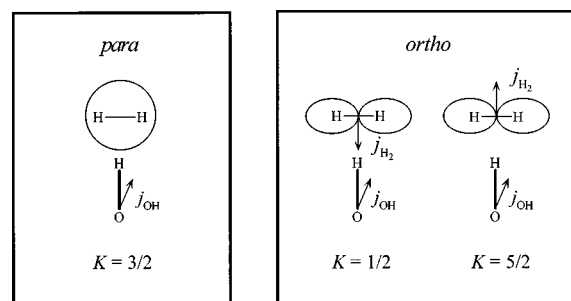


FIG. 1. Angular momentum vector addition model for *p*-H₂–OH and *o*-H₂–OH in the T-shaped minimum energy configuration. The intermolecular states are labeled by K , the projection of $j_{\text{OH}} + j_{\text{H}_2}$ (or equivalently J) on the intermolecular axis. For the *p*-H₂ complex, the ground state is predicted to be $K = 3/2$, derived from the projection of $j_{\text{OH}} = 3/2$ alone ($j_{\text{H}_2} = 0$). For the *o*-H₂ complex, vector addition of $j_{\text{OH}} = 3/2$ and $j_{\text{H}_2} = 1$ gives rise to $K = 1/2$ (ground state) or $5/2$.

constructed from the lowest energy free-rotor levels of OH and *p*-H₂, $j_{\text{OH}} = 3/2$ and $j_{\text{H}_2} = 0$, respectively. Higher rotational levels ($j_{\text{OH}} = 5/2, 7/2, \dots$ and $j_{\text{H}_2} = 2, 4, \dots$) contribute little to the character of the intermolecular bending states as a result of their large energy separations from the lowest rotor levels. The presence of the *p*-H₂ molecule lifts the $(2j + 1)$ orientational degeneracy of the $j_{\text{OH}} = 3/2$ rotational state of OH (${}^2\Pi_{3/2}, F_1$), giving rise to four angular states in *p*-H₂–OH (two $K = 3/2$ and two $K = 1/2$). For the T-shaped minimum energy configuration, in which the H of OH points toward the center-of-mass of H₂ and OH is oriented along the intermolecular axis, a simple angular momentum vector model predicts a $K = 3/2$ ground state. In this case, K is derived exclusively from the projection of $j_{\text{OH}} = 3/2$ on the intermolecular axis since $j_{\text{H}_2} = 0$, as illustrated schematically in Fig. 1.

For *o*-H₂–OH, the unquenched rotational angular momentum of *o*-H₂ ($j_{\text{H}_2} = 1$) provides an additional source of angular momentum not present in *p*-H₂–OH. In *o*-H₂–OH, the $(2j + 1) = 3$ degeneracy of H₂ as well as the $(2j + 1) = 4$ degeneracy of OH is lifted by the intermolecular potential. Accordingly, there are $3 \times 4 = 12$ different angular states that correlate with the lowest $j_{\text{H}_2} = 1$, $j_{\text{OH}} = 3/2$ rotational channel (two $K = 5/2$, four $K = 3/2$, and six $K = 1/2$). The T-shaped minimum energy configuration can result in either a $K = 1/2$ or $K = 5/2$ intermolecular state, arising from the vector addition of the projections of $j_{\text{OH}} = 3/2$ and $j_{\text{H}_2} = 1$ on the intermolecular axis. This is shown schematically using the vector model in Fig. 1. While these two intermolecular states are anticipated to be nearly degenerate for a given value of J , the requirement that $J \geq K$ causes the true ground state of *o*-H₂–OH to be $J = 1/2$, $K = 1/2$.

The other rigorously conserved quantity in OH–H₂ is total parity, p . All rovibrational states in OH–H₂ appear as pairs of levels with $+$ and $-$ parity. The energy level splitting between states of the same J and opposite parity arises primarily from differences in the energies of the A' and A'' PESs (i.e., the magnitude of V_{DIF}). There are additional interactions (Coriolis and spin decoupling) that contribute to the parity splitting, which in general make the splitting larger

in $K=1/2$ states as compared to $K>1/2$ states.⁴⁵ Intermolecular states of a given K that sample regions where V_{DIF} is large are expected to have a greater parity splitting than those that access regions where V_{DIF} is small. As a result, the magnitude and sign of the parity splitting in a particular intermolecular state provide information about the relative energies and ordering of the A' and A'' potentials in the region sampled by that state. This is particularly important since some of the excited intermolecular states accessed in this study are thought to sample regions of the PES where the sign and magnitude of V_{DIF} are very different from the region sampled by the ground intermolecular state.

Based on quantum calculations on the MCKW PES, the majority of *excited* intermolecular states for OH–H₂ involve bending motion (hindered internal rotation) of the constituent monomers. The only bound excited intermolecular stretching states are for *o*-H₂–OH at energies near the dissociation limit. Since the excited intermolecular bending states of *o*-H₂–OH correlate with $j_{\text{OH}}=3/2$ and $j_{\text{H}_2}=1$, the way one bending state can be differentiated from another is by its value of K . The bending states differ in how the angular momenta of the associated diatoms add together or, in other words, the relative orientation of the diatoms in the body-fixed frame of the complex. Thus, intermolecular excitation can be used to alter the “structure” of the OH–H₂ complex, thereby controlling the reagent approach geometry prior to both inelastic and reactive scattering events initiated in the complex by infrared excitation.

III. EXPERIMENT

A. Experimental method

As illustrated in Fig. 2, two different IR-UV double resonance techniques have been implemented to record the infrared overtone spectrum of OH–H₂ complexes, fluorescence depletion (FD) and fluorescence enhancement (FE). In both cases, the IR pump laser (bold arrow) is used to prepare the OH–H₂ complexes with two quanta of OH stretch, $v_{\text{OH}}=2$, as well as possible intermolecular excitation. In the FD method,³⁵ the UV' probe laser (dashed arrow) is fixed on a previously identified OH–H₂ electronic transition in the OH $A-X$ 1–0 region,^{32,33} giving rise to fluorescence. As the IR pump laser is scanned over an OH–H₂ rovibrational transition, the population in the ground state is reduced, causing a decrease in the UV' probe laser-induced fluorescence (LIF) signal.

In the FE experiment, the UV probe laser (solid arrow) is fixed on an OH–H₂ transition in the OH $A-X$ 1–2 or 2–2 region. When the IR pump laser is resonant with an OH–H₂ overtone transition, population is transferred to the $v_{\text{OH}}=2$ state. The UV laser then promotes the vibrationally activated OH–H₂ complexes to the excited A electronic state with $v_{\text{OH}}=1$ or 2, resulting in a probe LIF signal.

The IR laser used for these experiments is the idler output of a Continuum Powerlite 9010 Nd:YAG-pumped Sunlite BBO OPO operating at $\sim 1.4 \mu\text{m}$ with a 10 Hz repetition rate. The idler pulses are ~ 12 mJ/pulse with a bandwidth of 0.12 cm^{-1} and a duration of 4 ns. In the depletion experiments, the ultraviolet laser (UV') is the frequency-doubled

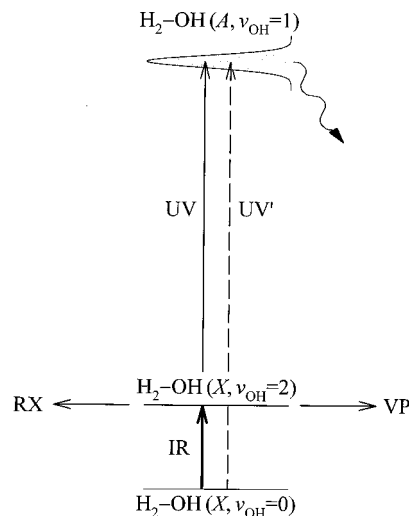


FIG. 2. Schematic diagram showing the two IR-UV double resonance schemes used to study OH–H₂. In the fluorescence depletion (FD) method, the UV' probe laser monitors the OH–H₂ ground state population ($v_{\text{OH}}=0$) via laser induced fluorescence (LIF). When the IR pump laser is resonant with a rovibrational transition of the complex, population is removed from the ground state resulting in a decrease in the LIF signal. In the fluorescence enhancement (FE) method, population transferred to rovibrational levels of the $v_{\text{OH}}=2$ state by the IR pump laser is detected by the UV probe laser via LIF. The vibrationally activated complex has sufficient energy to surmount the barrier to reaction (RX) or break the weak intermolecular bond via vibrational predissociation (VP).

output of a Nd:YAG-pumped dye laser running with Rhodamine 6G dye to excite the complex in the OH $A-X$ 1–0 region. The UV' laser pulses are 10 mJ/pulse, 6 ns in duration, and 0.08 cm^{-1} in bandwidth. For the enhancement experiments, the ultraviolet laser (UV) is *either* the frequency doubled output of a Nd:YAG-pumped dye laser operating with DCM dye in the OH $A-X$ 2–2 region *or* an excimer-pumped dye laser operating with Excalite 351 dye in the OH $A-X$ 1–2 region. The UV light generated from the YAG system has the same characteristics as UV' (10 mJ/pulse). The excimer-pumped dye laser has an output of ~ 6 mJ/pulse, a 0.25 cm^{-1} bandwidth, and a 20 ns pulse duration. All of the ultraviolet lasers operate at 20 Hz.

The OH–H₂ complexes are generated in a pulsed supersonic expansion of HNO₃ in 30% normal-H₂, balance He carrier gas at ~ 150 psi.^{32–35} The HNO₃ is photolyzed at 193 nm as the gas mixture flows through a quartz capillary tube that is attached to a pulsed valve which is cooled to 0 °C with a Peltier cooling chip. The IR and UV (or UV') lasers are counterpropagated through the vacuum apparatus, focused down to $\sim 1 \text{ mm}^2$, and intersect the expansion ~ 1.5 cm from the exit of the capillary. The lasers are synchronized such that the IR laser is present for every other UV (or UV') laser pulse, with the ultraviolet laser arriving in the interaction region 5–30 ns after the IR laser pulse. Both lasers are vertically polarized except when implementing the enhancement technique with the excimer-pumped dye laser system, in which case the UV laser is horizontally polarized. No effects due to laser polarization have been observed in the vibrational overtone spectra of OH–H₂.

The resultant fluorescence is imaged (f/1 lenses and spherical mirror) and filtered ($308 \pm 20 \text{ nm}$ bandwidth) prior

to detection with a photomultiplier tube (PMT). The LIF signal is then preamplified, integrated, and transferred to a computer for analysis. On alternating pulses, the LIF signal arising from the ultraviolet laser only (SIG1) or that resulting from the presence of both the IR and ultraviolet lasers (SIG2) is collected. The depletion spectra are recorded by evaluating the UV' LIF signal ratio $[(\text{SIG1} - \text{SIG2})/\text{SIG1}] \times 100\%$ at each IR laser frequency step. Fluorescence enhancement spectra are obtained by comparing the UV LIF signal with and without IR excitation, $\text{SIG2} - \text{SIG1}$, as the IR laser is scanned.

During each IR-UV double resonance scan, the signal output (~ 471.5 nm) from the OPO was passed through an étalon (4.17 mm thick, 0.8202 cm^{-1} free spectral range). The étalon trace was used to determine the relative frequencies of the individual transitions and to linearize the infrared spectra. A decrease in the IR idler power at 6971.319 cm^{-1} , due to an atmospheric water absorption line, provided an absolute calibration of the infrared spectra. In addition, the absolute frequency of the idler output from the OPO was checked by recording a H_2O photoacoustic spectrum in the $1.4\text{ }\mu\text{m}$ region. The photoacoustic spectrum was assigned according to previously published water transitions.⁴⁶

The state-selective lifetimes for vibrationally excited OH-H_2 were measured in the time-domain using a variation of the fluorescence enhancement method. The vibrationally activated OH-H_2 complex decays via reaction (RX) or vibrational predissociation (VP), as illustrated in Fig. 2. For these measurements, the delay between the IR and UV lasers was stepped in 5 ns increments using an EG&G digital delay generator, with the frequencies of the OPO and excimer-pumped dye lasers fixed on OH-H_2 transitions. The enhancement signal was accumulated for 200 (100 IR on, 100 IR off) shots at each time delay, yielding a time profile for OH-H_2 in specific rovibrational states. The lifetime was extracted from the data by fitting the time profile to a single exponential decay curve convoluted over a Gaussian excitation pulse with a FWHM of 4 ns. The lifetime measurements were repeated multiple times in order to obtain statistically significant uncertainties.

B. Comparison of FD and FE methods

The fluorescence depletion and enhancement techniques each have their own advantages and disadvantages for recording IR-UV double resonance spectra. Both techniques utilize the fluorescence (or ionization) signal induced by an electronic transition of the complex as a means of detecting the infrared (or stimulated Raman) spectrum for that species. The depletion method is more generally applicable,⁴⁷⁻⁵⁶ as it does not rely on any prior knowledge of the transition frequencies or lifetimes of the vibrationally excited levels. The IR laser can be scanned without limit to search for new rovibrational transitions. Fluorescence depletion, however, is not a zero background method. In order to observe the infrared transitions, the IR pump laser must induce depletions in the UV laser-induced fluorescence signal that are larger than baseline fluctuations. Typically, this requires significant absorption strength on the vibrational transition and a high flux of IR photons. Depletions in excess of 50% can be obtained

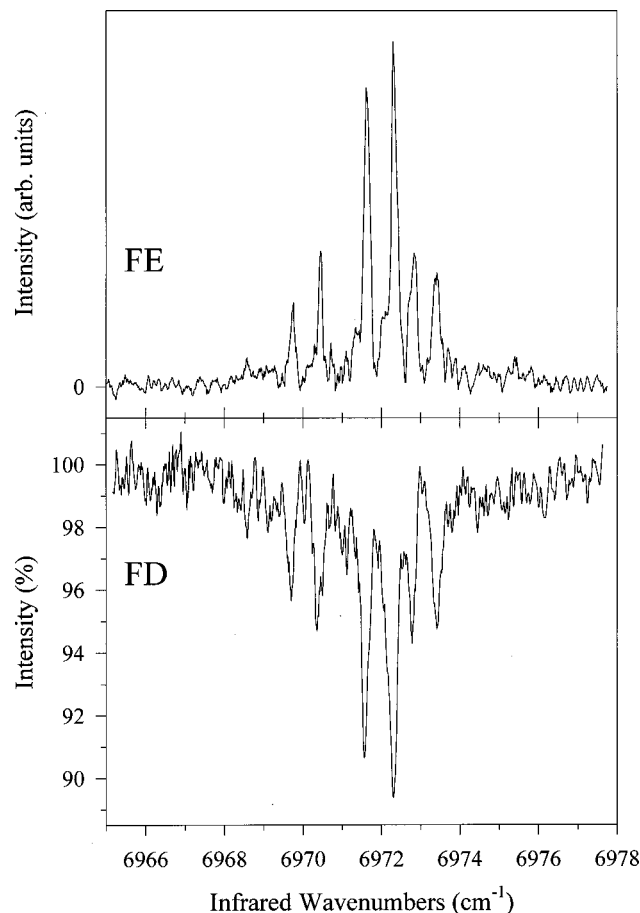


FIG. 3. Rotationally resolved infrared spectrum of the pure OH overtone band of $o\text{-H}_2\text{-OH}$ recorded via fluorescence enhancement (FE) and fluorescence depletion (FD). The baseline fluctuations in the infrared spectrum detected via FE are substantially reduced compared to the FD detected spectrum. See text for details.

if the upper state lifetime is short compared to the IR pulse width, circumventing the two-level saturation limit.

The depletion method was used to record the infrared spectrum of the pure overtone band of OH-H_2 shown in Fig. 3. For this scan, the UV' laser was fixed on an OH-H_2 electronic transition in the OH $A-X$ 1-0 region ($35\,408\text{ cm}^{-1}$). Note the $\pm 1\%$ fluctuations in the 100% baseline level (no IR induced transitions) even after signal averaging 300 shots (150 IR on, 150 IR off) per point, which arise from the pulse-to-pulse variations in the pulsed valve, excimer photolysis laser, and UV' probe laser. Fluorescence depletions as large as 11% were achieved when pumping overtone transitions originating from single rotational and parity levels of the ground state of OH-H_2 , e.g., the $Q(1/2)^-$ line at 6972.27 cm^{-1} .

By contrast, fluorescence enhancement is a zero background technique.^{48,49} In the absence of the IR pump laser, there is no population in vibrationally excited OH-H_2 levels and therefore no UV laser-induced fluorescence signal arising from OH-H_2 . The enhancement method was used to record the infrared spectrum of OH-H_2 shown in Fig. 3. Here, the UV probe laser was fixed on an OH-H_2 transition in the OH $A-X$ 2-2 region at $31\,255\text{ cm}^{-1}$, while the IR laser was scanned through the pure overtone band of

o-H₂-OH. In the enhancement mode, the gain of the PMT is increased and the baseline fluctuations arise from scattered light.

For many systems, the enhancement technique will *not* be the method of choice when searching for new transitions. Implementation can be technically challenging since the IR and UV lasers need to be scanned synchronously, one increased and the other decreased in frequency, in order to maintain the resonance condition in the excited electronic state.⁵⁷ In the case of OH-H₂, however, the electronic transition excited by the UV probe laser is extensively homogeneously broadened,^{32,33} as indicated by the shaded region in Fig. 2. This broadening allows the IR pump laser to be scanned over 50 cm⁻¹ without having to adjust the UV probe laser frequency. This is a fortuitous characteristic of the OH-H₂ system, enabling a search for combination bands involving intermolecular excitation using the enhancement method.

The fluorescence enhancement method works well when the vibrationally excited state is long-lived relative to the IR laser duration, as is the case for OH-H₂. Furthermore, the lifetime of the vibrationally excited state can be measured directly in the time-domain by varying the delay between the IR excitation pulse and the UV probe laser. On the other hand, if the intermediate state lifetime is significantly shorter than the laser pulses, then the enhancement signal will be reduced in amplitude or may not even be observable, as found for OH-D₂.⁵⁸

IV. RESULTS AND ANALYSIS

A. Pure overtone via fluorescence enhancement

The rotationally resolved infrared spectrum of the pure OH overtone stretch (no intermolecular excitation) was originally recorded using the FD technique.³⁵ This spectrum is repeated here using fluorescence enhancement with the UV laser fixed on an OH-H₂ electronic transition in the OH A-X 1-2 or 2-2 regions. In the 1-2 region, the UV laser is fixed at 28 498 cm⁻¹, which is near the peak of feature H in Ref. 32 (taking into account the IR excitation energy). In the 2-2 region, the UV laser is fixed at 31 255 cm⁻¹. In both cases the optimum UV laser frequency was empirically determined based on the magnitude of the signal on the $Q(1/2)^-$ line in the OH-H₂ infrared enhancement signal. No discernible difference is observed in the infrared spectra recorded with the UV laser fixed in the 2-2 or 1-2 regions. The pure overtone spectrum recorded with the UV laser fixed in the 2-2 region is shown in Fig. 3. No transitions due to OH monomer or H₂O are observed due to the double resonance condition used to record these spectra.

The rotational structure of the pure overtone stretch is dominated by a strong central *Q*-branch with a large parity splitting. This band was previously assigned as a $K=1/2 \leftarrow 1/2$ band of *o*-H₂-OH based on a detailed comparison with *ab initio* theory.³⁵ The origin is at 6971.9 cm⁻¹, shifted 0.6 cm⁻¹ to higher energy from that of the uncomplexed OH. The frequencies of the infrared transitions determined from the fluorescence enhancement spectrum are identical (to within the experimental precision of ± 0.05 cm⁻¹) to the in-

frared transition frequencies determined previously using the FD method.³⁵ Furthermore, the relative intensities of the individual rovibrational transitions in the infrared spectra recorded using FD and FE are remarkably similar (see Fig. 3). This is consistent with the vibrationally averaged structures for the $v_{OH}=0$ and $v_{OH}=2$ states of OH-H₂ being quite similar and, therefore, the Franck-Condon factors for the electronic transitions used in depletion and enhancement measurements should also be nearly equal.

If the vibrationally averaged structure of OH-H₂ is altered by infrared excitation, for example through excitation of combination bands involving intermolecular vibrations, then the Franck-Condon factors for the electronic transitions utilized in the enhancement and depletion experiments may differ. This could cause certain intermolecular states (for a specific UV transition) to be more or less prominent in the FE detected infrared spectrum compared to the spectrum recorded via FD. For OH-H₂, combination bands that involve intermolecular excitation are more easily observed with FE detection and, as a result, this method is used exclusively for characterizing the combination bands of OH-H₂.

B. Combination band spectroscopy

Infrared scans up to 60 cm⁻¹ higher in energy of the pure overtone origin reveal approximately 20 additional rovibrational transitions, which are shown in Fig. 4. These newly identified transitions are believed to be combination bands that access excited intermolecular states supported by the OH ($X^2\Pi, v=2$) + H₂ potential. The first combination band transition is observed 9.9 cm⁻¹ to higher energy of the pure overtone, with additional transitions detected nearly up to the OH ($v=2$) + H₂ dissociation limit ($D_0 \approx 54$ cm⁻¹).³³ The transitions are relatively sparse (~ 1 transition/2 cm⁻¹) consistent with the large pseudodiatom *B* rotational constant for OH-H₂. In contrast, no transitions were observed to lower energy of the pure overtone.

An important issue in assigning the transitions is the possibility that both *o*-H₂-OH and *p*-H₂-OH could be contributing to the observed spectrum. On the time scale of the supersonic expansion, we assume that the *o*- and *p*-H₂ nuclear spin states do not interconvert. Thus, an ideal supersonic expansion of normal-H₂ should result in 25% $j=0$ (*p*-H₂) and 75% $j=1$ (*o*-H₂). The *o*-H₂-OH and *p*-H₂-OH complexes are distinct species with different infrared spectra. There is no evidence that the electronic transition used in the detection scheme preferentially probe either the ortho or para complex, and the infrared spectrum of these two complexes should overlap. However, there are several reasons why the infrared spectrum shown in Fig. 4 is attributed to *o*-H₂-OH.

First, the nuclear spin weights of *o*-H₂ and *p*-H₂ suggest that there should be *three* *o*-H₂-OH complexes for every *one* *p*-H₂-OH complex. This makes *o*-H₂-OH easier to detect. Second, the best available theoretical calculations predict that *o*-H₂-OH is bound by 45 cm⁻¹ compared to the 28 cm⁻¹ binding energy of *p*-H₂-OH.³⁶ Preferential complexation due to this difference in binding energy can further increase the ortho/para ratio in the OH-H₂ complex. Any *p*-H₂-OH complex that is formed in the expansion can be

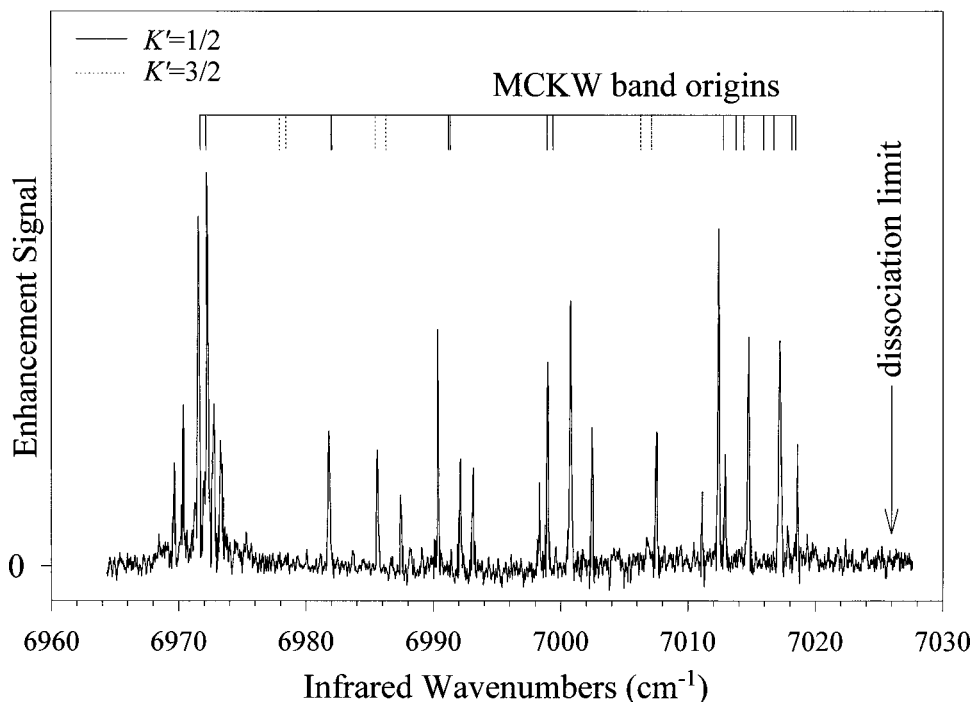


FIG. 4. Infrared spectrum of *o*-H₂-OH recorded via the IR-UV fluorescence enhancement (FE) method. The pure overtone band is centered around 6972 cm⁻¹ and the transitions towards higher energy are combination bands involving simultaneous excitation of the OH overtone and intermolecular bending vibrations. The ticks at the top of the spectrum are the line positions of *Q*-branch transitions from a fully *ab initio* calculation of the infrared spectrum based on the MCKW potential (Ref. 36). Ticks are shown for both parity components of the lowest allowed $\Delta J=0$ transition from the ground $K=1/2$ state to each intermolecular state. The experimentally determined dissociation energy is indicated with an arrow.

converted to *o*-H₂-OH by collisions with *o*-H₂ and subsequent displacement of the *p*-H₂. Thus, complexation can enrich the ortho to para ratio in the complex, making it even harder to detect the *p*-H₂-OH complex. Third, combination band transitions with appreciable oscillator strength are predicted³⁶ to extend out to the dissociation limit for *o*-H₂-OH, in qualitative agreement with the ~ 47 cm⁻¹ span of the experimental spectrum. By contrast, the para complex is predicted to have combination band transitions extending only 10–15 cm⁻¹ higher in energy than the pure overtone. Finally, in the pure overtone region where the S/N is the highest, *p*-H₂-OH has not been observed in either the depletion or enhancement spectra. Thus, while it is possible that some of the transitions in Fig. 4 are due to *p*-H₂-OH, all of the experimental measurements to date strongly suggest that the infrared spectrum is entirely due to *o*-H₂-OH.

C. Combination band rovibrational assignments

The cold jet conditions ($T_{\text{tot}} \leq 10$ K) and large rotational constant for OH-H₂ give rise to only a few lines for each band, making a rovibrational assignment of the *o*-H₂-OH combination bands difficult. The large parity splitting for most intermolecular states results in additional transitions, but even so an entire “band” in Fig. 4 may consist of only a couple transitions. Nevertheless, some progress can be made in assigning the spectrum using the bound state calculations based on the MCKW *ab initio* potential.³⁶ The transition frequencies of the combination bands observed are listed in Table I, along with tentative assignments. When possible, these tentative rovibrational assignments can be tested using

the ground state combination differences determined from the pure overtone spectrum³⁵ (see examples below). In addition, based on the pure overtone band, we expect *Q*-branch transitions to be stronger than the associated *R*- and *P*-branch transitions.

The frequencies of the *Q*-branch transitions for the lowest *J* of both parities for each *o*-H₂-OH combination band can be predicted from the bound state calculations.³⁶ An adiabatic separation of the high-frequency OH stretch and low-frequency intermolecular coordinates has been assumed in the 4D quantum calculations, with the OH and H₂ bond lengths fixed at their ground vibrational state values. This approximation should be valid since the origin of the pure overtone band of OH-H₂ is shifted by less than 1 cm⁻¹ relative to that of uncomplexed OH. Thus, we assume that the intermolecular states observed experimentally for the excited vibrational state ($\nu_{\text{OH}}=2$) can be compared directly with the intermolecular states calculated for the ground state surface ($\nu_{\text{OH}}=0$). The calculated eigenvalues are used to predict far-infrared transition frequencies, which are then shifted by the experimentally determined origin for the pure overtone band (6971.92 cm⁻¹).³⁵ The predicted transition frequencies of the *Q*-branch (lowest allowed *J*) for intermolecular states with $K=1/2$ and $3/2$ are presented as ticks in the upper part of Fig. 4.

Based on the MCKW *ab initio* calculations, the first combination band feature observed at 6981.78 cm⁻¹ is assigned to overlapping parity components of the *Q*(1/2) transitions that terminate on an excited $K=1/2$ bending level. The excited level is assigned as a $K=1/2$ state because the

TABLE I. Experimental transition frequencies (cm^{-1}) for $o\text{-H}_2\text{-OH}$ measured via fluorescence enhancement. The *ab initio* transition frequencies, upper state K , and rovibrational assignments are based on 4D quantum calculations on the MCKW potential (Ref. 36).

Experiment		<i>ab initio</i>	
Frequency	Frequency	K	Assignment
6971.55	6971.5	1/2	$Q(1/2)^+$ Ground state
6972.27	6972.4	1/2	$Q(1/2)^-$ Ground state
6981.78	6982.0	1/2	$Q(1/2)^{+/-}$
6983.65			
6985.57	6985.8	3/2	$Q(3/2)^-$
6987.42	6986.4	3/2	$Q(3/2)^+$
6988.20	6988.1	3/2	$R(1/2)^-$
6989.07	6988.7	1/2	$P(3/2)^+$
6990.33	6991.3	1/2	$Q(1/2)^{+/-}$
6992.10	6993.6	1/2	$R(1/2)^+$
6993.12	6994.8	1/2	$R(1/2)^-$
6998.34	6999.2	1/2	$Q(3/2)^-$
6998.98	6998.9	1/2	$Q(1/2)^+$
6999.60			
7000.76	6999.4	1/2	$Q(1/2)^-$
7002.49	7000.2	1/2	$Q(3/2)^+$
7007.59			
7011.13			
7012.39			
7012.93			
7014.73			
7017.20			
7017.80			
7018.58			

calculated intermolecular energy, 10.1 cm^{-1} , agrees remarkably well with the experimentally measured intermolecular energy, 9.86 cm^{-1} , the difference between the peak frequency and the OH-H_2 pure overtone origin. The calculations indicate that the ordering of parity levels for this excited bending state are reversed compared to the ground intermolecular level. The Q -branch ($\Delta J=0$, $p' \neq p''$) then will involve transitions between lower-lower and upper-upper parity levels. The calculations predict that the parity splitting in the excited $K=1/2$ bending level is 0.53 cm^{-1} , while in the ground state it is 0.46 cm^{-1} (both $J=1/2$). Therefore, the quantum calculations predict that the two parity components of the $Q(1/2)$ transitions will overlap to within $<0.1 \text{ cm}^{-1}$, consistent with the single unresolved peak that is observed. For this excited intermolecular state, therefore, *ab initio* theory appears to reproduce both the intermolecular energy and parity splitting.

In comparing experiment and theory, it is also important to identify when theory predicts intermolecular states where no transitions are observed. The only situation where this occurs is for the lowest energy calculated $K=3/2$ intermolecular bending state. The $Q(3/2)$ transitions that access this state are predicted at $Q(3/2)^+ = 6978.5 \text{ cm}^{-1}$ and $Q(3/2)^- = 6977.9 \text{ cm}^{-1}$, yet no transitions are observed in this region (see Fig. 4). Transitions to this intermolecular level may have a small infrared oscillator strength or poor Franck-Condon overlap for the electronic transition used in the detection, consequently making these transitions too weak to be observed experimentally at the present S/N. Alternatively,

this discrepancy could be due to inaccuracies in the MCKW potential.

The next higher energy combination band is assigned to a $K=3/2 \leftarrow 1/2$ band where the transitions at 6985.57 cm^{-1} and 6987.42 cm^{-1} are assigned to the $Q(3/2)^-$ and $Q(3/2)^+$ lines, respectively. Theory predicts an excited $K=3/2$ intermolecular bending state at 6986.1 cm^{-1} (14.2 cm^{-1}) and these two lines are centered about 6986.50 cm^{-1} (14.58 cm^{-1}), with intermolecular energies given in parentheses. Consistent with this assignment and the previously determined ground state combination differences,³⁵ a weak $R(1/2)^-$ transition is identified at 6988.20 cm^{-1} . Specifically, the ($J=3/2^- - J=1/2^-$) ground state combination difference (CD) was measured to be 2.60 cm^{-1} in the pure overtone,³⁵ while here it is 2.63 cm^{-1} , i.e., within the $\pm 0.05 \text{ cm}^{-1}$ frequency precision of the experiment. This assignment predicts the $R(1/2)^+$ transition at 6988.62 cm^{-1} , but no peak is detected. Since the frequency difference between the two $Q(3/2)$ lines (1.85 cm^{-1}) is greater than the experimentally determined parity splitting in the ground state (1.0 cm^{-1} for $J=3/2$), the ordering of the parity levels in the upper state appears to be the same as in the ground state. This is opposite to the ordering of the parity levels predicted for this excited $K=3/2$ state.

The quantum calculations indicate that the next higher energy bending state is a $K=1/2$ level at an intermolecular energy of 19.3 cm^{-1} (6991.3 cm^{-1}). Similar to the other excited $K=1/2$ intermolecular level, this state is calculated to have a parity splitting of comparable magnitude but opposite sign to the ground state, and thus the two parity components of the $Q(1/2)$ transitions are predicted to overlap. The relatively strong line at 6990.33 cm^{-1} (18.41 cm^{-1}) is assigned as the unresolved parity components of the $Q(1/2)$ transition to this $K=1/2$ intermolecular bending state. The two transitions towards higher energy at 6992.10 and 6993.12 cm^{-1} are assigned as $R(1/2)^+$ and $R(1/2)^-$ lines, respectively. Since no $Q(3/2)$ lines are observed, the $R(1/2)$ assignments cannot be tested using ground state combination differences. However, a weak $P(3/2)^+$ line at 6989.07 cm^{-1} is identified using combination differences ($\text{CD}=1.20$ vs 1.26 cm^{-1}), which is consistent with this rovibrational assignment. Assuming a $3B$ spacing between the $Q(1/2)$ and $R(1/2)$ lines (averaged over parity components) the excited state B rotational constant is approximately 0.76 cm^{-1} . This value is significantly larger than the experimentally measured³⁵ ground state rotational constant of 0.63 cm^{-1} , and corresponds to a 0.33 \AA decrease in the vibrationally averaged center-of-mass separation (R) of the OH and H_2 subunits in a pseudodiatom model. Similarly, the quantum calculations predict an increase in B from 0.66 to 0.97 cm^{-1} , which is also consistent with a decrease in R for this state. The change in sign of the parity splitting along with the contraction in the intermolecular separation is anticipated for an intermolecular state that samples a local minimum identified on the intermolecular potential, which will be discussed in greater detail in Sec. V B.

The Q -branch for another $K=1/2$ intermolecular state is predicted at 6999.2 cm^{-1} (27.2 cm^{-1}) and two lines are observed centered around 6999.87 cm^{-1} (27.95 cm^{-1}). This state is predicted to have a small positive parity splitting (i.e., the same ordering as ground state) that should lead to resolvable Q -branch parity components. The four lines centered around 7000 cm^{-1} are thus assigned as the $Q(1/2)$ and $Q(3/2)$ transitions. This assignment is consistent with the upper state having a large parity splitting of around 1.3 cm^{-1} in the $J=1/2$ state, which is larger than the ground state $J=1/2$ parity splitting of $\sim 0.5\text{ cm}^{-1}$. This is not consistent, however, with the magnitude of the parity splitting ($<0.1\text{ cm}^{-1}$) calculated for this $K=1/2$ state.

Finally, we did not attempt to assign the remaining ~ 8 transitions to higher energy since these are most likely due to several intermolecular bending (and possibly stretching) states near the dissociation limit. Quantum calculations predict five intermolecular states within 10 cm^{-1} of the dissociation limit. Thus, the rotational progressions for these states are expected to be strongly perturbed due to Coriolis forces and angular-radial coupling in the potential. The observed features extend up to the predicted dissociation limit and cut off abruptly approximately 47 cm^{-1} to higher energy of the pure overtone origin. Scans as much as 20 cm^{-1} to higher energy than the last observed feature at 7018 cm^{-1} did not reveal any additional features. This is strong circumstantial evidence that the abrupt end to the combination band transitions is due to excitation above the dissociation limit ($D_0=54\text{ cm}^{-1}$).

The agreement between experiment and theory on the intermolecular energies is very good and suggests that the average MCKW *ab initio* potential (V_{AVG}) is reproducing the basic topology of the intermolecular potential energy surface. Of the OH-H_2 states with intermolecular energies below 30 cm^{-1} , only the $K=3/2$ combination band at 6978 cm^{-1} (6.3 cm^{-1}) is not observed, as discussed above. Other differences between experiment and theory are measured, in particular, the sign and magnitude of the parity splitting in excited intermolecular states. These discrepancies most likely reflect inaccuracies in the difference potential (V_{DIF}). Currently, we are performing analogous experiments⁵⁸ using OH-D_2 to check the tentative rovibrational assignments presented here and to further test the MCKW potential.

D. OH-H_2 lifetime measurements

As discussed in Sec. III B, another advantage of the fluorescence enhancement scheme is that it permits the lifetime of the vibrational excited state to be measured directly in the time domain. A time profile for $o\text{-H}_2\text{-OH } \nu_{\text{OH}}=2$ obtained by pumping the $Q(1/2)^-$ line of the pure overtone band is displayed in Fig. 5. This trace was recorded by varying the time delay ($\Delta t=t_{\text{UV}}-t_{\text{IR}}$) between the IR pump and UV probe lasers in 5 ns increments, with the IR pump and UV probe lasers operating at 6972.3 cm^{-1} and 28498 cm^{-1} , respectively, in the enhancement mode. As seen in Fig. 5, no LIF signal is observed when the UV laser arrives in the interaction region in advance of the IR pump laser. The signal

then rises rapidly to a maximum when the IR and UV lasers are overlapped in time (and space). At longer delays, the fluorescence signal falls off with a single exponential decay profile.

These data are well described by a least squares fit of a simple exponential decay function with a unimolecular decay rate $k=1/\tau$,

$$S(\Delta t)=A \exp(-\Delta t/\tau), \quad (1)$$

convoluted over a Gaussian excitation function with a FWHM of 4 ns. As shown in Fig. 5, the individual lifetimes determined from the fit are reasonably precise ($\pm 10\text{ ns}$). Repeated measurements of the $Q(1/2)^-$ time profiles yield a lifetime of $\tau=115(26)\text{ ns}$, where the uncertainty in the parentheses is the 2σ value for 12 repeated measurements, not the uncertainty of an individual fit. Additionally, measurements of the OH monomer $\nu=2$ vibrational state lifetime ($\tau_{\text{rad}}\approx 50\text{ ms}$) (Ref. 59) showed that the signals are constant for $\sim 300\text{ ns}$ before starting to decay due to translational motion of the excited OH molecules out of the UV probe region. Thus, we are confident that the measured decays for $o\text{-H}_2\text{-OH } \nu_{\text{OH}}=2$ reflect the excited state lifetime. Lifetime measurements for a few of the stronger combination band lines indicate that some of the excited intermolecular states may have even longer lifetimes, as great as $\tau=200\text{ ns}$. However, it is difficult to measure long-lived states in the fast moving He/H₂ expansions. Currently, we are employing another double resonance scheme to measure vibrational excited state lifetimes and product state distributions; these results will be published elsewhere.^{60,61}

V. DISCUSSION

A. Decay dynamics of vibrationally activated OH-H_2

Vibrational overtone excitation prepares the OH-H_2 entrance channel complexes with two quanta of OH stretch as well as a specified amount of intermolecular vibrational ex-

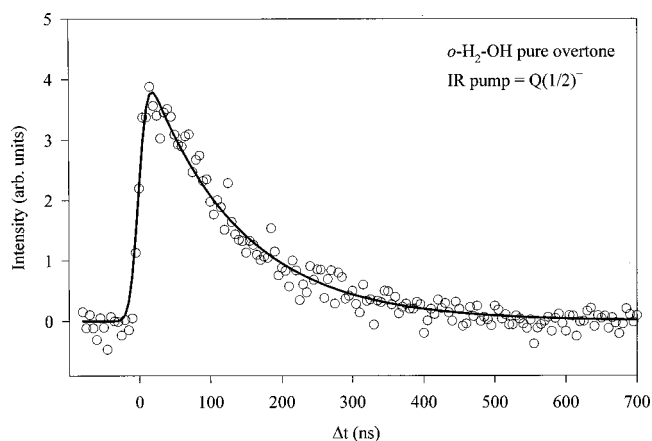


FIG. 5. Representative time trace of vibrationally activated OH-H_2 recorded via the enhancement mode. The line is the result of a least squares fit of the data to Eq. (1) convoluted over a Gaussian excitation pulse. This data is plotted as a function of the time delay (Δt) between the UV probe laser and the IR pump laser. The IR laser pumps the $Q(1/2)^-$ line of the pure OH vibrational overtone, with the UV laser operating at 28498 cm^{-1} . Based on repeated measurements, the $o\text{-H}_2\text{-OH } (\nu_{\text{OH}}=2)$ lifetime is determined to be $\tau=115(26)\text{ ns}$.

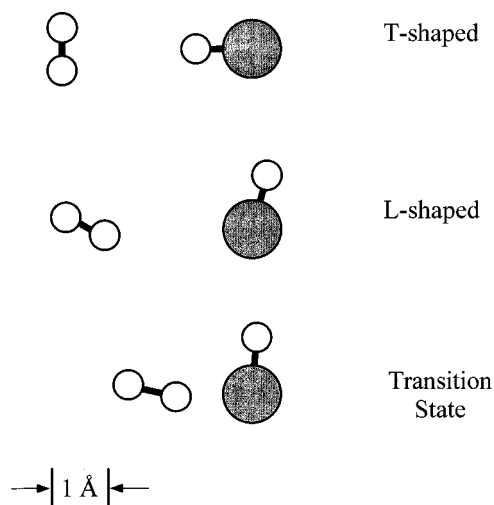


FIG. 7. OH-H₂ structures at the T-shaped global minimum (-188 cm^{-1}) and L-shaped local minimum (-168 cm^{-1}) on the average MCKW *ab initio* potential (Ref. 36). Atom-atom distances are drawn to scale, with O atoms displayed as filled circles and H atoms as open circles. Included is the *ab initio* calculated structure of the transition state for the OH+H₂ reaction (Ref. 41).

energy level pattern is not consistent with that observed experimentally. First, the KF potential predicts that the ground state of *o*-H₂-OH is a $K=3/2$ state, whereas the experimental evidence indicates the ground state is a $K=1/2$ level.³⁵ In addition, transitions are observed to intermolecular levels that lie $10\text{--}20\text{ cm}^{-1}$ higher in energy than the ground state where *no* intermolecular states are predicted for the KF potential. Furthermore, the infrared spectrum calculated using the KF potential predicts that the *o*-H₂-OH spectrum should span approximately 80 cm^{-1} , with particularly strong combination band transitions appearing $\sim 60\text{ cm}^{-1}$ to higher energy of the pure overtone (see Fig. 10 in Ref. 36). In contrast to these predictions, the combination band transitions observed experimentally range only over $\sim 47\text{ cm}^{-1}$. Finally, the calculated $D_0=85\text{ cm}^{-1}$ on the KF potential seriously overestimates the experimental binding energy of 54 cm^{-1} determined from electronic spectroscopy.³³ All of this information taken together is rather convincing proof that the KF potential does not accurately reproduce the topology of the OH+H₂ intermolecular potential in the entrance channel.

A closer examination of the “shapes” of these two *ab initio* potentials reveals why their intermolecular energy level patterns and infrared spectra are predicted to be so different from one another. Both potentials exhibit minima in T-shaped and near L-shaped configurations. The T-shaped minimum is derived from electrostatic interactions (dipole-quadrupole and quadrupole-quadrupole) and has been discussed in detail for OH-H₂ elsewhere.³⁶ Analogous T-shaped minima are found on the intermolecular potentials of H₂-HF and H₂-HCl.⁶⁵ The L-shaped minimum seems to arise from attractive interactions of the lone π -electron of the OH radical with molecular hydrogen on the reactive (*A'*) surface. The orientation of the OH and H₂ reactants in the near L-shaped configuration is remarkably similar to the transition state structure calculated for the chemical

reaction,⁴¹ aside from the intermolecular separation distance, as shown in Fig. 7.

The global minimum ($V_{\text{AVG}}=-188.1\text{ cm}^{-1}$) on the MCKW average potential occurs in the T-shaped configuration with $R=3.22\text{ Å}$. The L-shaped local minimum ($V_{\text{AVG}}=-168.0\text{ cm}^{-1}$) appears at a shorter value of $R=2.90\text{ Å}$ with $\theta_{\text{OH}}=102^\circ$, $\theta_{\text{H}_2}=29^\circ$, where θ_{OH} and θ_{H_2} are the polar angles of OH and H₂, respectively. These two configurations are illustrated in Fig. 7 and the coordinates of the two minima are given in Table II. In contrast, the KF potential predicts that the near L-shaped orientation ($\theta_{\text{OH}}=112^\circ$, $\theta_{\text{H}_2}=20^\circ$) is the global minimum ($V_{\text{AVG}}=-322.1\text{ cm}^{-1}$), where as the T-shaped configuration is significantly higher in energy ($V_{\text{AVG}}=-245.8\text{ cm}^{-1}$, see Table II). This fundamental difference in the topology of the two surfaces is responsible for the qualitatively different intermolecular energy level patterns and associated infrared spectra calculated for each surface.

As discussed in Sec. IV C, there is spectroscopic evidence that the excited intermolecular states accessed in this study sample regions of the potential surface far from the T-shaped global minimum. For the combination band at 6990 cm^{-1} there is evidence of a contraction in the intermolecular bond length and a change in the sign of the parity splitting. This would be consistent with an excited intermolecular state that samples the secondary L-shaped minimum, where the minimum occurs at a shorter intermolecular bond length and the sign of the V_{DIF} is opposite to that in the T-shaped configuration. In addition, the $K=1/2$ excited state at 6982 cm^{-1} exhibits parity split levels with opposite sign, but comparable magnitude, as the ground state. Once again, this indicates that the *A'* surface is lower in energy than *A''* in the region of the PES sampled by this state.

The OH-H₂ system provides the opportunity to study intermolecular forces in an open-shell reactive complex. The intermolecular potential for OH-H₂ differs from those for the closed shell analogs H₂-HF and H₂-HCl, in that there are distinct potential energy surfaces of *A'* (reactive) and *A''* (nonreactive) symmetry. Additional *ab initio* calculations, particularly for the near-L-shaped configuration, would be helpful to better determine the form of the *A'* and *A''* PESs in this region.

C. Implications for reactive potentials

The reactive (*A'*) component of the MCKW PES is plotted as a function of intermolecular separation distance R in Fig. 8 for the T-shaped and L-shaped orientations shown in Fig. 7. The *A'* surface exhibits an attractive well in both

TABLE II. Coordinates of the T-shaped and L-shaped potential minima on the MCKW (Ref. 36) and KF (Ref. 38) potential energy surfaces. Polar angles are in degrees and potential energies are in cm^{-1} .

		$R/\text{Å}$	θ_{OH}	θ_{H_2}	V_{AVG}	V_{DIF}
MCKW	T-shaped	3.22	0.0	90.0	-188.1	-8.9
KF	T-shaped	3.12	0.0	90.0	-245.8	-6.1
MCKW	L-shaped	2.90	101.7	28.6	-168.0	40.6
KF	L-shaped	2.77	111.5	19.0	-322.1	3.6

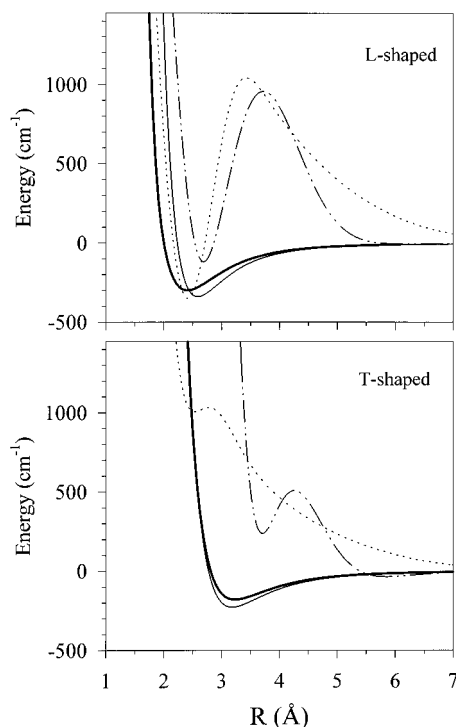


FIG. 8. Radial cuts of the reactive component (A') of various *ab initio* potentials for OH-H_2 in the L-shaped and T-shaped orientations shown in Fig. 7. The infrared spectroscopy results have verified the shape of the MCKW potential (bold solid line) in the attractive well regions. The entrance channel regions of other potentials are shown for comparison; KF potential (solid line), unmodified SE potential (dot-dash line), and S5 surface (dotted line). Note that both reactive potentials (SE and S5) predict a large unphysical barrier in the L-shaped configuration. See text for details.

orientations (see also Table II). For the T-shaped orientation the minimum on the A' surface occurs at $R = 3.1 \text{ \AA}$, while for the L-shaped configuration the attractive well is deeper and the minimum occurs at a smaller R -value. The infrared spectroscopy results have verified the shape of this *ab initio* potential in the attractive well region. For comparison, the A' component of the KF potential in these configurations is also shown in Fig. 8. Although the shapes of the KF and MCKW potentials look quite similar, the KF potential is not consistent with the experimental results (see Sec. V B).

Also shown in Fig. 8 are the entrance channels for the OH+H_2 reactive surfaces (SE and S5) plotted as a function of R for the same T- and L-shaped orientations with the OH and H_2 bond lengths fixed at their asymptotic values. The “spurious” well located in the entrance channel of the SE PES is evident in both of these configurations. This well is thought to result from limitations in the form of the analytical potential function used to fit the *ab initio* data, which causes ripples in certain areas of the PES. Modified versions of the SE potential have been developed that reduce this effect, particularly in the L-shaped orientation.^{10,11}

In the T-shaped geometry, the SE surface supports a slight well at large R ($\sim 5.8 \text{ \AA}$) followed by a repulsive interaction at shorter R that shows a dip around 3.75 \AA . The repulsive wall is at $\sim 3.5 \text{ \AA}$ on the SE surface compared to a value of $< 3 \text{ \AA}$ for the MCKW potential. The S5 surface predicts a purely repulsive interaction in the T-shaped geom-

etry that dips slightly at $R = 2.5 \text{ \AA}$. The discrepancy between the potentials developed for reactive studies and the MCKW potential is even greater for the L-shaped configuration. As the reactants approach one another with an L-shaped orientation on the SE potential, there is a barrier of $\sim 1000 \text{ cm}^{-1}$ at $R = 3.5\text{--}4.0 \text{ \AA}$ in the entrance channel and then the potential dips below 0 cm^{-1} before rising steeply again. For the L-shaped configuration, the S5 surface is very close in form to the SE potential.

Neither reactive surface accurately reproduces the shape of the OH+H_2 potential in the entrance channel to reaction, where the MCKW potential has been shown to be qualitatively correct. The SE potential has been modified^{10,11} to improve the form of the potential in the entrance channel and eliminate the spurious well in the L-shaped configuration, which causes sharp resonances in quantum reactive scattering calculations. As newer surfaces are developed for this reaction, the present results should provide a useful guide for the shape of the OH+H_2 potential in the entrance channel.

VI. CONCLUSIONS

This paper reports the infrared spectrum of $o\text{-H}_2\text{-OH}$ in the OH overtone region, consisting of the pure OH overtone band and many combination bands which extend out to the OH ($v = 2$) + $o\text{-H}_2$ dissociation limit. The infrared spectrum provides detailed experimental information on the energies of the intermolecular bending states in the ground electronic state of $o\text{-H}_2\text{-OH}$ $v_{\text{OH}} = 2$. When compared with 4D quantum simulations, this data provides a rigorous means for sensitively probing the entrance channel to the OH+H_2 reaction. The spectroscopic data clearly indicates that the MCKW *ab initio* potential³⁶ is more consistent with experiment than the older KF PES.^{37,38} Further experimental information on the topology of the OH-H_2 PES and the identity of the intermolecular bending states is being explored through infrared spectroscopy of the OH-D_2 isotopomer.⁵⁸ It is our hope that the present experiments will stimulate more theoretical work on the intermolecular PES and bound intermolecular states of OH-H_2 .

The vibrationally activated $o\text{-H}_2\text{-OH}$ complex in the $v_{\text{OH}} = 2$ state is found to be quite long-lived. The 115(26) ns lifetime is ascribed to the amount of time that the initial OH stretching excitation remains localized in the OH bond. Vibrational excitation of the OH “spectator” bond is not expected to dramatically enhance reaction, even though the $\sim 7000 \text{ cm}^{-1}$ of excitation is more than sufficient to surmount the barrier to reaction. The long lifetime does not exclude the possibility that reaction is occurring, however, as the measured lifetime is inversely related to the sum of the reaction and vibrational predissociation decay rates. The branching ratio will be needed to determine the relative rates for these two channels. In contrast to OH vibrational activation, excitation of the H_2 moiety within the complex may result in large reaction rates for favorable configurations, since both experiment and theory have shown that the cross section for reaction is dramatically increased for bimolecular collisions of OH with H_2 ($v = 1$).^{1,3,4,19} Stimulated Raman studies are currently underway in this laboratory to measure the lifetime of the $v_{\text{H}_2} = 1$ excited vibrational state in

OH–H₂. It is hoped that by measuring the mode- and isotopomer-selective lifetimes of OH–H₂ excited vibrational states, we can gain a better understanding of how different forms of energy and different intermolecular bending states (reagent approach geometries) affect the rate of reaction in this benchmark system.

ACKNOWLEDGMENTS

This work has been supported by grants from the Chemistry Division of the National Science Foundation and the Office of Basic Energy Sciences of the Department of Energy. The authors thank Steven M. Miller and David C. Clary (University College, London) for helpful discussions and for supplying us with their 4D bound state code for OH–H₂.

- ¹G. C. Light and J. H. Matsumoto, *Chem. Phys. Lett.* **58**, 578 (1978).
- ²F. P. Tully and A. R. Ravishankara, *J. Phys. Chem.* **84**, 3126 (1980).
- ³G. P. Glass and B. K. Chaturvedi, *J. Chem. Phys.* **75**, 2749 (1981).
- ⁴R. Zellner and W. Steinert, *Chem. Phys. Lett.* **81**, 568 (1981).
- ⁵A. R. Ravishankara, J. M. Nicovich, R. L. Thompson, and F. P. Tully, *J. Phys. Chem.* **85**, 2498 (1981).
- ⁶M. Alagia, N. Balucani, P. Casavecchia, D. Stranges, and G. G. Volpi, *J. Chem. Phys.* **98**, 2459 (1993).
- ⁷M. Alagia, N. Balucani, P. Casavecchia, D. Stranges, G. G. Volpi, D. C. Clary, A. Kliesch, and H.-J. Werner, *Chem. Phys.* **207**, 389 (1996).
- ⁸A. Sinha, M. C. Hsiao, and F. F. Crim, *J. Chem. Phys.* **92**, 6333 (1990).
- ⁹M. J. Bronikowski, W. R. Simpson, and R. N. Zare, *J. Phys. Chem.* **97**, 2194 (1993).
- ¹⁰D. C. Clary, *J. Chem. Phys.* **95**, 7298 (1991).
- ¹¹D. C. Clary, *J. Chem. Phys.* **96**, 3656 (1992).
- ¹²D. C. Clary, *Chem. Phys. Lett.* **192**, 34 (1992).
- ¹³J. Echave and D. C. Clary, *J. Chem. Phys.* **100**, 402 (1994).
- ¹⁴S. K. Pogrebnya, J. Echave, and D. C. Clary, *J. Chem. Phys.* **107**, 8975 (1997).
- ¹⁵J. M. Bowman and D. Wang, *J. Chem. Phys.* **96**, 7852 (1992).
- ¹⁶D. Wang and J. M. Bowman, *J. Chem. Phys.* **96**, 8906 (1992).
- ¹⁷D. H. Zhang and J. Z. H. Zhang, *J. Chem. Phys.* **99**, 5615 (1993).
- ¹⁸D. H. Zhang and J. Z. H. Zhang, *J. Chem. Phys.* **101**, 1146 (1994).
- ¹⁹D. H. Zhang and J. Z. H. Zhang, *J. Chem. Phys.* **100**, 2697 (1994).
- ²⁰D. H. Zhang and J. Z. H. Zhang, *J. Chem. Phys.* **102**, 7400 (1995).
- ²¹H. Zhang and J. Light, *J. Chem. Phys.* **105**, 1291 (1996).
- ²²W. Zhu, J. Q. Dai, J. Z. H. Zhang, and D. H. Zhang, *J. Chem. Phys.* **105**, 4881 (1996).
- ²³D. Neuhauser, *J. Chem. Phys.* **100**, 9272 (1994).
- ²⁴U. Manthe, T. Seideman, and W. H. Miller, *J. Chem. Phys.* **101**, 4759 (1994).
- ²⁵H. Szichman and M. Baer, *J. Chem. Phys.* **101**, 2081 (1994).
- ²⁶S. P. Walch and T. H. Dunning, Jr., *J. Chem. Phys.* **72**, 1303 (1980).
- ²⁷G. C. Schatz and H. Elgersma, *Chem. Phys. Lett.* **73**, 21 (1980).
- ²⁸W. H. Thompson, H. O. Karlsson, and W. H. Miller, *J. Chem. Phys.* **105**, 5387 (1996).
- ²⁹D. C. Clary, J. K. Gregory, M. J. T. Jordan, and E. Kauppi, *J. Chem. Soc., Faraday Trans.* **93**, 747 (1997).
- ³⁰A. D. Isaacson, *J. Chem. Phys.* **107**, 3832 (1997).
- ³¹E. de Beer, E. H. Kim, D. M. Neumark, R. F. Gunion, and W. C. Lineberger, *J. Phys. Chem.* **99**, 13627 (1995).
- ³²R. A. Loomis and M. I. Lester, *J. Chem. Phys.* **103**, 4371 (1995).
- ³³R. A. Loomis, R. L. Schwartz, and M. I. Lester, *J. Chem. Phys.* **104**, 6984 (1996).
- ³⁴R. A. Loomis and M. I. Lester, *Annu. Rev. Phys. Chem.* **48**, 643 (1997).
- ³⁵R. L. Schwartz, D. T. Anderson, M. W. Todd, and M. I. Lester, *Chem. Phys. Lett.* **273**, 18 (1997).
- ³⁶S. M. Miller, D. C. Clary, A. Kliesch, and H. J. Werner, *Mol. Phys.* **83**, 405 (1994).
- ³⁷E. Kochanski and D. R. Flower, *Chem. Phys.* **57**, 217 (1981).
- ³⁸S. M. Miller and D. C. Clary, *J. Chem. Phys.* **98**, 1843 (1993).
- ³⁹T. H. Dunning, Jr., L. B. Harding, A. F. Wagner, G. C. Schatz, and J. M. Bowman, *Science* **240**, 453 (1988).
- ⁴⁰J. M. Bowman and G. C. Schatz, *Annu. Rev. Phys. Chem.* **46**, 169 (1995).
- ⁴¹E. Kraka, J. Gauss, and D. Cremer, *J. Chem. Phys.* **99**, 5306 (1993).
- ⁴²P. Andresen, H. Häusler, and H. W. Lülf, *J. Chem. Phys.* **81**, 571 (1984).
- ⁴³P. Andresen, N. Aristov, V. Beushausen, D. Häusler, and H. W. Lülf, *J. Chem. Phys.* **95**, 5763 (1991).
- ⁴⁴A. R. Offer and M. C. van Hemert, *J. Chem. Phys.* **99**, 3836 (1993).
- ⁴⁵W. H. Green, Jr. and M. I. Lester, *J. Chem. Phys.* **96**, 2573 (1992).
- ⁴⁶R. A. Toth and J. S. Margolis, *J. Mol. Spectrosc.* **55**, 229 (1975).
- ⁴⁷R. H. Page, Y. R. Shen, and Y. T. Lee, *J. Chem. Phys.* **88**, 4621 (1988).
- ⁴⁸G. V. Hartland, B. F. Henson, V. A. Venturo, R. A. Hertz, and P. M. Felker, *J. Opt. Soc. Am. B* **7**, 1950 (1990).
- ⁴⁹P. M. Felker, P. M. Maxton, and M. W. Schaeffer, *Chem. Rev.* **94**, 1787 (1994).
- ⁵⁰P. M. Maxton, M. W. Schaeffer, S. M. Ohline, W. Kim, V. A. Venturo, and P. M. Felker, *J. Chem. Phys.* **101**, 8391 (1994).
- ⁵¹P. M. Maxton, M. W. Schaeffer, and P. M. Felker, *Chem. Phys. Lett.* **241**, 603 (1995).
- ⁵²W. S. Kim and P. M. Felker, *J. Chem. Phys.* **107**, 2193 (1997).
- ⁵³R. N. Pribble and T. S. Zwier, *Faraday Discuss.* **97**, 229 (1994).
- ⁵⁴R. K. Frost, F. C. Hagemeister, C. A. Arrington, D. Schleppendach, T. S. Zwier, and K. D. Jordan, *J. Chem. Phys.* **105**, 2605 (1996).
- ⁵⁵T. S. Zwier, *Annu. Rev. Phys. Chem.* **47**, 205 (1996).
- ⁵⁶A. P. Milce, D. E. Heard, R. E. Miller, and B. J. Orr, *Chem. Phys. Lett.* **250**, 95 (1996).
- ⁵⁷A. P. Milce and B. J. Orr, *J. Chem. Phys.* **104**, 6423 (1996).
- ⁵⁸M. W. Todd, D. T. Anderson, and M. I. Lester (in preparation).
- ⁵⁹D. D. Nelson, Jr., A. Schiffman, D. J. Nesbitt, and D. J. Yaron, *J. Chem. Phys.* **90**, 5443 (1989).
- ⁶⁰J. M. Hossenlopp, D. T. Anderson, M. W. Todd, and M. I. Lester, *J. Chem. Phys.* (submitted).
- ⁶¹P. J. Krause, D. C. Clary, D. T. Anderson, M. W. Todd, R. L. Schwartz, and M. I. Lester, *Chem. Phys. Lett.* (in press).
- ⁶²K. J. Rensberger, J. B. Jeffries, and D. R. Crosley, *J. Chem. Phys.* **90**, 2174 (1989).
- ⁶³K. M. Beck, M. T. Berry, M. R. Brustein, and M. I. Lester, *Chem. Phys. Lett.* **162**, 203 (1989).
- ⁶⁴R. E. Miller, *Science* **240**, 447 (1988).
- ⁶⁵D. C. Clary and P. J. Knowles, *J. Chem. Phys.* **93**, 6334 (1990).